Graphene based ZnO nanoparticles to depolymerize lignin-rich residues via UV/iodide process

Mazarji, Mahmoud; Alvarado-Morales, Merlin; Tsapekos, Panagiotis; Nabi-Bidhendi, Gholamreza; Mahmoodi, Niyaz Mohammad; Angelidaki, Irini

Published in:
Environment International

Link to article, DOI:
10.1016/j.envint.2018.12.062

Publication date:
2019

Document Version
Publisher's PDF, also known as Version of record

Environment International 125 (2019) 172–183

Contents lists available at ScienceDirect

Environment International

journal homepage: www.elsevier.com/locate/envint

Graphene based ZnO nanoparticles to depolymerize lignin-rich residues via UV/iodide process

Mahmoud Mazarji[a,b], Merlin Alvarado-Morales[a], Panagiotis Tsapekos[a], Gholamreza Nabi-Bidhendi[b], Niyaz Mohammad Mahmoodi[c], Irini Angelidaki[a,*]

[a] Department of Environmental Engineering, Technical University of Denmark, Kgs. Lyngby, DK-2800, Denmark
[b] School of Environment, College of Engineering, University of Tehran, Tehran, Iran
[c] Department of Environmental Research, Institute for Color Science and Technology, Tehran, Iran

ARTICLE INFO

Handling Editor: Thanh Nguyen

Keywords:
UV/Iodide
Lignin degradation
Graphene
Phenolics

ABSTRACT

In this work, potassium iodide (KI) and graphene oxide (GO) were utilized to promote the selectivity of photocatalytic process for alkali lignin oxidation over ZnO. Different concertation of GO was added during the microwave synthesis procedure of ZnO, and the characterization results revealed that graphene can shift the conduction band to more reducing potential, resulting to higher production of superoxide anion radicals ($O_2\cdot^-$) compared to ·OH. Response Surface Methodology revealed the most suitable interaction among loading of GO, KI and irradiation time on lignin and total phenolic compound (TPC) degradation. Specifically, the optimal conditions (*i.e.* maximum lignin (52%) and minimum TPC (55%) degradation) were at [KI] = 0.64 mM; GO content into ZnO 1.2 mg/mL; 240 min of irradiation time. The results showed that higher addition of graphene into structure of ZnO could preserve more phenolics from degradation due to less production of ·OH. Furthermore, the addition of KI at optimized conditions could enhance the selectivity of degradation of lignin and phenolics *via* producing I· radicals and quenching the excess amount of generated ·OH, respectively. The lower generation of ·OH at optimized conditions was quantitatively confirmed by a photoluminescence simplified technique. In addition, the effect of the photocatalytic process on substrate's anaerobic degradability was examined in order to evaluate the suitability of the pretreated solution for energy recovery. Indeed, besides the higher TPC concentration, the biogas production of treated straw at optimized conditions was increased by 35% compared to the untreated sample.

1. Introduction

Lignin represents a major component of lignocellulosic biomass with high aromaticity. If treated properly, it can potentially decompose to form valuable products (*e.g.*, phenol, benzene, toluene, and xylene) that can replace petro-chemical analogues and ensure a sustainable supply of the carbon feedstock for energy and chemical industry (Den et al., 2018). To transform lignin into polymers of interest, a proper treatmnet method must be selected aiming at valorizing as much as possible of lignin into a range of several value-added molecules. Among various existing treatment methods for valorisation, advanced photocatalytic oxidation process is a potential new transformation technology for lignin derivatives to value added products (Awungacha Lekelefac et al., 2015). It is well-known that photocatalytic oxidation of lignin-rich residues is characterized as non-selective processes, causing challenging the photocatalytic transformation of lignin into valuable chemicals. Specifically, numerous studies have shown that ·OH radicals produced during the photocatalytic reaction are considered as the main reactive species (Felício et al., 2003; H. Li et al., 2015; Kansal et al., 2008; Lu et al., 2014; Ma et al., 2008; Nair et al., 2016; Portjanskaja et al., 2009; Song et al., 2015). Furthermore, it has been shown previously that the phenolic compounds are the major lignin derivatives during photocatalytic oxidation strategies (Alvarado-Morales et al., 2017; Chen et al., 2018; Gong et al., 2017; Nair et al., 2016; Prado et al., 2013; Tsapekos et al., 2018). The ideal process should thus be able to steadily decompose lignin and continuously preserve high-value small molecule compounds. However, side reactions inevitably occur due to the ability of ·OH radicals to engage in the oxidation of

Abbreviations: CT, charge transfer; ED, electron donor; CTTS, charge-transfer-to-solvent; TPC, total phenolic compound; RSM, Response Surface Methodology; CCD, central composite design; BMP, biochemical methane potential

* Corresponding author.
E-mail address: iria@env.dtu.dk (I. Angelidaki).

https://doi.org/10.1016/j.envint.2018.12.062
Received 13 November 2018; Received in revised form 19 December 2018; Accepted 29 December 2018

phenolics, leading to rather gaseous products (Al-Hamdi et al., 2015; Y. Li et al., 2015; Liu et al., 2017; Sheng et al., 2014). In order to address this issue, a photocatalytic reaction has to be able to decrease generation of ·OH radicals to avoid overoxidation of value-added chemicals without compromising lignin degradation yield.

Several strategies for modification of photocatalysts have been developed which can decrease the formation of ·OH. These methods are including band gap modification, selective growth of crystal facets, and surface treatment (Kou et al., 2017). The goal for enhancing the photocatalytic selectivity can be accomplished by compositing a semiconductor with the recently fast-developed carbonaceous materials in the nanotechnology field. As a two-dimensional monoatomic-thick sheet of hexagonally arranged carbon, graphene has become the focus of interest in multiple disciplines due to its superior properties, including large theoretical specific surface area (~2600 m^2/g), remarkable thermal conductivity (5000 W/(m·K)), and high carrier mobility (200,000 $cm^2/(V·s)$) (Julkapli and Bagheri, 2015; Kumar et al., 2017). Recent development has shown that the accumulation of electrons as result of the presence graphene increases the Fermi level of the semiconductor to more negative potential, causing the composite system to be more reductive than the pristine semiconductor system (Subramanian et al., 2004; Wang et al., 2013). Thus, it is expected for the composite to have less oxidation potential in the valence band, limiting production of non-selective ·OH. In this regard, fabricated composites may be candidates for reduced generation of ·OH during photocatalytic lignin degradation.

In spite of above-mentioned advantages of graphene in UV/semiconductor system, avoiding the generation of strong, non-selective ·OH would decrease the overall efficiency of process. Hence, the compensation for ·OH in photocatalytic process must be taken into consideration. In this sense, Iodide photolysis under UV illumination (UV/Iodide) can contribute to the production of hydrated electrons ($e_{aq}-$) and iodine radical (I·) by charge-transfer-to-solvent (CTTS) mechanism, leading direct degradation of many recalcitrant materials (Sun et al., 2017). In addition, iodide can act as a sacrificial electron donor (ED). In this system, the primary role of ED is to form a charge transfer (CT) complex between the semiconductor and a sacrificial ED in order to react irreversibly with the photogenerated valence band holes, thus prohibiting the generation of ·OH (Li et al., 2011; Song et al., 2007).

The principal objective of this study was to prove the hypothesis of controlling the generation of ·OH by potassium iodide (KI) and graphene oxide (GO) utilization for promoting the selectivity of photocatalytic process for alkali lignin decomposition. The effect of different loading of GO into semiconductor structure during varying iodide concentration upon UV irradiation was investigated. Among different semiconductors widely employed, we used zinc oxide (ZnO) due to its promising potential for environmental remediation especially in the case of lignin photocatalytic degradation (Gouvêa et al., 2000; H. Li et al., 2015; Kansal et al., 2008; Villaseñor and Mansilla, 1996). Response Surface Methodology (RSM) as a multivariate statistical technique was used for modeling and optimization of the experiments with three factors including GO content into ZnO structure, initial KI concentration, and irradiation time. In addition, the pretreated materials were anaerobically digested in order to evaluate the suitability of the photocatalytic solution for energy recovery purposes.

2. Materials and methods

2.1. Materials

Sigma-Aldrich Kraft lignin, abbreviated as lignin, was purchased from Sigma-Aldrich (product number 370959). The surrounding area of Copenhagen (Zealand, Denmark) was chosen to collect wheat straw residues. A cutting mill (SM 200, Retsch GmbH, Germany) was used to cut the fibers to < 0.5 cm. Subsequently, the resulting fibers were sieved in order to obtain a homogeneous particle size of 18 mesh (1 mm). Other chemicals in this study were obtained from Sigma-Aldrich and used as received without further purification.

2.2. Photocatalyst preparation

The modified Hummers' method was followed for synthesizing graphite oxide nanosheets (Hosseinabadi-Farahani et al., 2015). To prepare ZnO nanorods incorporated with graphene, a microwave method was adopted. In brief, the graphite oxide powder was dispersed in deionized water (1 mg/mL) to obtain a suspension. Then, the suspension was ultra-sonicated by probe sonication (Branson, Digital Sonifier Model 250) for 10 min (10 s on pulse and 40 s off, with 50% power) to obtain graphene oxide suspension. Finally, the suspension was centrifuged at 8000 rpm for 10 min to obtain graphene oxide (GO) powder. The GO was dried at 60 °C for 24 h before use. 36 mg of GO were dispersed into 10 mL deionized water. Then, a 2 g zinc chloride ($ZnCl_2$) dissolved in 10 mL deionized water and then, the $ZnCl_2$ solution was dropwise added to the GO solution. The resulting solution was kept at stirring for 8 h to ensure a good contact between Zn^{2+} and GO. Thereafter, 10 mL of ammonia 25% w/w solution was mixed with the aforementioned solution very slowly. The resultant solution comprising of 0.5 M $ZnCl_2$ and 1.2 mg/mL GO in final volume of 30 mL aqueous solution was transferred into Teflon-sealed autoclave and underwent microwave irradiation (Anton Paar, multiwave 3000) at a power of 600 W for 30 min at the temperature of 160 °C with stirring. The participates at the bottom of microwave-irradiated solution were allowed to cool down to the room temperature and recovered by filtration. Then, they were washed thoroughly with ethanol/water and fully dried overnight. The final powder was designated as ZnO-G1.2. In order to find an optimum condition for synthesis of ZnO-graphene composite (ZnO-G) which can promote selective photocatalytic activity, different loadings of GO into ZnO composition were applied. To achieve increased selectivity, concentrations of GO (*i.e.* 0.2, 0.6, 0.95 GO mg/mL) was varied following the same procedure, at fixed concentration of 0.5 M $ZnCl_2$. The final products designated as ZnO-Gx, which x was accounted as the concentration of GO used in the composite. The pure ZnO was also synthesized in accordance to aforementioned steps without addition of GO.

2.3. Characterization of photocatalyst

Scanning electron microscopy (SEM) using a FEI Quanta 200 FEG was employed to investigate the morphology of nanoparticles. The crystallite phase of materials was detected by X-ray diffraction (XRD) using Cu-Ka radiation operating at 40 mA and 45 kV (X'Pert Pro, Panalytical). The functional groups were studied by Fourier transform infrared spectroscopy (FTIR) using a Spectrum One spectrophotometer (Nicolet iS50, Thermo Fisher Scientific). Thermal gravimetric analysis (TGA) using a Discovery TGA from TA Instruments in a temperature range from 25 to 900 °C at scan rate of 10 °C/min was utilized to study the thermal properties of the synthesized materials. Furthermore, Raman spectroscopy was recorded from 1000 to 2000 cm^{-1} on an Almega Thermo Nicolet Dispersive Raman Spectrometer operating at wavelength of 514 nm. For investigating optical properties of as-prepared materials, Ultraviolet-visible (UV–vis) spectra (UV–vis spectrophotometer Perkin–Elmer Lambda 25) were utilized. Valence band spectra were performed by X-ray photoelectron spectroscopy (XPS) using Specs model EA10 plus (Bestec Co, Germany) using Al as a radiation source. Active oxidative species (·OH radicals) generated on the surface of photocatalysts were evaluated by a photoluminescence (PL) simplified technique to quantitatively analyze the relative production of ·OH during irradiation of samples containing terephthalic acid (TA). It is well known that TA readily reacts with ·OH to produce a highly fluorescent product, 2-hydroxyterephtahalic acid (TAOH) in alkaline systems (Jimenez-Relinque and Castellote, 2015). In a typical PL experiment, 0.5 mM of TA was dispersed into 50 mL alkaline solution

(2 mM of NaOH) at the optimized conditions without addition of lignin. Then, the solution was exposed to UV light for 30 min. After separating the photocatalyst, the resultant solution was analyzed on a Fluorescence Spectrophotometer (EClips CARY VARIAN PL) through measuring the PL intensity at excitation of λ_{exc} = 315 nm and emission of λ_{emi} = 425 nm.

2.4. Photocatalytic experiments

The photocatalytic experiment was carried out in a beaker placed at a quasi-collimated beam apparatus equipped with the doped medium pressure lamp (SR HUV700, 700 W, Scan Research A/S, Denmark) with increased emission at low wavelength. A detailed description of the reactor setup and lamp characteristics can be found in an earlier work (Hansen et al., 2013). Air was sparged to assure the availability of sufficient amount of oxygen in the reactor during photocatalytic trials. Samples preparation for the photocatalytic experiments began with the overnight soaking of 0.01 g of lignin in 100 mL solution formed by 25 mM NaOH solution and distilled water. In a typical procedure of photocatalysis, 0.005 g of the photocatalyst and desired concentration of KI were added to the resulting lignin solution. The mixture was mixed in dark conditions for 1 h to ensure the establishment of adsorption-desorption equilibrium under darkness. After this period, the UV lamp was turned on for the desired time span. At certain time intervals, 2 mL samples were collected and centrifuged. The supernatant was collected for further examinations.

2.5. Response surface modeling

The central composite design (CCD) was employed to investigate the photocatalytic degradation of lignin. The RSM was used for evaluation of interactive effects of GO content into ZnO matrix (x_1), initial KI concentration (x_2) and irradiation time (x_3) on the photocatalytic degradation process, while other affecting factors such as oxygen supply, agitation speed, temperature, lignin concentration, and photocatalyst dosage were kept constant during the process. The ranges of independent variables and experimental conditions derived from CCD are summarized in Table 1. Total number of experiments carried out was 20, consisting of six axial, eight factorial and six center points. Table 2 provides the detail of the 20 experimental conditions.

A second-order model as shown in Eq. (1) was used to correlate the degradation efficiency expressed in lignin and TPC as a function of the three independent variables:

$$Y = \beta_0 + \sum_{i=1}^{n} \beta_i x_i + \sum_{i=1}^{n} \beta_{ii} x_i^2 + \sum_{i=1}^{n} \sum_{j=i+1}^{n} \beta_{ij} x_i x_j \quad (1)$$

where, Y (%) represents the predicted response; x_i and x_j are the coded i and jth independent variable; β_o, β_i, β_{ii}, and β_{ij} are the intercept, the first-order model coefficient, the quadratic coefficient of variable i, and the interaction coefficient of variables i and j, respectively. The reliability of fitted model was judged by the based on the analysis of variance (ANOVA) and as well as the coefficient of determination (R^2). The statistical analysis software JMP Pro 13 (SAS Institute Inc.) was used to build and analyze the second-order polynomial model.

After developing the second-order polynomial model, optimum solution for experimental variables (x_i) are achieved in which the response output becomes maximum and minimum for degradation of lignin and TPC, respectively.

Table 1
Experimental ranges and levels of independent variables.

Variables	Factors	Unit	Ranges and levels				
			−1.68	−1	0	+1	+1.68
A: GO	x_1	mg/mL	0	0.24	0.60	0.96	1.20
B: KI	x_2	mM	0	0.20	0.50	0.80	1
C: Time	x_3	min	40	80.54	140	199.46	240

2.6. Wheat straw photocatalytic experiment and biochemical methane potential (BMP) assays

To gain more knowledge about increasing bioavailability of residue after photocatalytic oxidation, lignin was replaced with wheat straw as real biomass feedstock. The lignin content of wheat straw was 26.7 ± 2.4%TS. The more detailed characterizations can be found elsewhere (Tsapekos et al., 2017). Experiments were carried out in a similar procedure to photocatalytic lignin degradation at the optimized conditions except increasing the loading of the substrate to 1 g/L. The treated residue after photocatalysis was recovered through a filter (GF/C Whatman® glass microfiber filter), and followed by oven-drying at 50 °C for 24 h for performing FTIR and SEM analysis.

The influence of the photocatalytic treatment on wheat straw and lignin biodegradability was assessed by means of batch anaerobic digestion experiments before and after photocatalysis. The anaerobic inoculum was collected from a lab-scale reactor fed with cattle manure and municipal waste. The detailed characteristics can be found in previous study (Tsapekos et al., 2018). The tests were conducted under thermophilic conditions (55 ± 1 °C) following the guidelines of Angelidaki et al. (2009). Batch reactors made of glass vessels with a total volume of 238 mL and a working volume of 120 mL were used. The organic load was kept at 1.5 gVS/L. Prior to incubation, the batch reactors were flushed with a N_2/CO_2 (80/20% (v/v)) gas mixture, closed with rubber stoppers and aluminum caps to ensure anaerobic conditions. During the incubation period, the reactors were shaken once a day to avoid the development of dead zones.

2.7. Analytical methods

The lignin concentration was measured on a spectrophotometer (UV–vis spectrophotometer UH5300 Hitachi) at the maximum absorbance of lignin at a wavelength of 280 nm originated predominantly from benzenoid compounds (Kobatakawa et al., 1989). A calibration graph was constructed based on plotting absorbance *vs.* concentration to quantify the lignin concentration in alkaline medium using Beer–-Lambert's law. The concentration of total phenolic compound (TPC) was determined quantifiably based on the Folin-Ciocalteu method (Ainsworth and Gillespie, 2007). A calibration plot was constructed to quantify the TPC content using Gallic acid as standard. The phenolic molecules produced after photocatalysis in the liquid phase were analyzed and qualified with a gas chromatography/mass spectrometry (GC/MS, Agilent 7890A/5975C). The analysis conditions were selected as follows: a capillary column was used (HP-INNOWAX, 30 m × 0.25 mm × 0.25 μm) at programmed oven temperature of 60 °C, hold for 2 min at 60 °C and then ramped up at a rate of 10 °C/min to 260 °C and hold at this level for extra 10 min; the injector was kept at 280 °C in spit mode with spit ratio of 1:2; helium was used as the carrier gas. The methane concentration in the headspace of batch reactors was determined using a gas chromatograph (Thermo Scientific™, Trace™ 1310) as previously described (Khoshnevisan et al., 2018). For the degradability experiments, the methane yields were reported at standard temperature and pressure (STP) conditions.

3. Results and discussion

3.1. Photocatalyst characterizations

SEM images of as-prepared ZnO and ZnO-G1.2 nanocomposites are presented in Fig. 1a and b. From Fig. 1a, it can be clearly observed the pure ZnO is composed of numerous rods in hexagonal shape. As can be seen, the added GO could act as nucleation sites for growth and formation of ZnO (Fig. 1b). ZnO particles were distributed well and each

Table 2
CCD design matrix for three variables with observed and predicted values for TPC and lignin degradation.

Run order	Coded values			Real values			TPC degradation (%)		Lignin degradation (%)	
	x_1	x_2	x_3	A: GO (mg/mL)	B: KI (mM)	C: Time (min)	Exp. TPC (%)	Pred. TPC (%)	Exp. lignin (%)	Pred. lignin (%)
1	−1	−1	−1	0.24	0.20	80.54	41.45	41.58	4.36	5.51
2	−1	+1	+1	0.24	0.80	199.46	75.28	75.79	50.51	50.95
3	+1	−1	+1	0.96	0.20	199.46	76.03	75.90	39.43	38.41
4	+1	−1	−1	0.96	0.20	80.54	41.25	41.39	7.59	6.00
5	−1.68	0	0	0.00	0.50	140.00	67.38	69.13	30.93	30.75
6	0	0	0	0.60	0.50	140.00	65.73	66.19	28.97	29.79
7	−1	+1	−1	0.24	0.80	80.54	51.25	53.37	12.11	16.14
8	0	0	0	0.60	0.50	140.00	65.73	66.19	28.00	29.79
9	0	0	0	0.60	0.50	140.00	67.50	66.19	30.00	29.79
10	+1.68	0	0	1.20	0.50	140.00	62.23	63.25	26.52	28.83
11	0	0	0	0.60	0.50	140.00	70.00	66.19	32.00	29.79
12	0	0	−1.68	0.60	0.50	40.00	32.78	31.17	3.13	1.14
13	0	0	0	0.60	0.50	140.00	65.00	66.19	31.00	29.79
14	0	−1.68	0	0.60	0.00	140.00	56.60	57.59	11.58	13.89
15	−1	−1	+1	0.24	0.20	199.46	76.83	76.09	39.59	37.92
16	+1	+1	+1	0.96	0.80	199.46	67.13	68.99	46.32	48.18
17	0	0	+1.68	0.60	0.50	240.00	79.33	79.06	56.98	57.66
18	0	0	0	0.60	0.50	140.00	67.50	66.19	32.00	29.79
19	0	+1.68	0	0.60	1.00	140.00	64.55	61.69	34.66	31.04
20	+1	+1	−1	0.96	0.80	80.54	45.18	46.56	12.87	13.38

particle was entirely coated by the Gr sheet intimately. These intimate contact facilities the electronic interaction between ZnO and graphene; thus, endows the composite with many excellent properties (Fan et al., 2012). In addition, Fig. S1 shows the photograph of the ZnO-Gx nanocomposites taken after the microwave reduction process. The color of white powder of ZnO becomes darker as the amount of GO content increases, indicating the higher content of GO successfully loaded into ZnO structure and well deoxygenated and reduced to graphene. Fig. 1c shows the XRD patterns of ZnO and ZnO-G1.2 to analyze their crystalline phase. The feature diffraction peak of both ZnO and ZnO-G1.2 exhibit similar diffraction peaks of (100), (002), (101), (102), (110), and (103) which correspond to a typical pattern of hexagonal phase Wurtzite ZnO (JCPDS card No. 36-1451). However, no typical diffraction peaks belonging to the graphene appear for the composite, which indicates that the disordered stacking of graphene was formed in the composite (Li et al., 2012). It also supports the conclusion that ZnO nanorods were successfully adsorbed on the surface of graphene nanosheets, which prevented the stacking of graphene nanosheets. TGA measurements were performed in the temperature range from 25 °C to 900 °C and the resulting curves are shown in Fig. 1d. The thermogram of ZnO exhibited better thermal stability compared to ZnO-G1.2. The composite showed 10% weight loss relative to ZnO which can be attributed to the amount of graphene in ZnO-G1.2 loaded into ZnO structure.

3.2. Model development and validation

A CCD design, of 20 experiments, was carried out in order to explore the effects of three independent variables on degradation efficiency of lignin and TPC (as responses). The actual and predicted responses are listed in Table 2. The regression equations were obtained by fitting experimental results to quadratic model. For both responses, the final mathematical models associated to the response in terms of actual factors after elimination of insignificant terms (p-value > 0.05) are expressed by Eqs. (2) and (3). The final equations in terms of coded factors are given by Eqs. (S1) and (S2) in Supporting information.

$$\begin{aligned} \textit{Lignin degradation} = {} & 29.79 - 0.96 \times \left(\frac{(GO - 0.6)}{0.6}\right) + 8.58 \times \left(\frac{KI - 0.5}{0.5}\right) \\ & + 28.26 \times \left(\frac{(Time - 140)}{100}\right) + \left(\frac{(GO - 0.6)}{0.6}\right) \\ & \times \left(\left(\frac{KI - 0.5}{0.5}\right) - 2.30\right) + \left(\frac{(KI - 0.5)}{0.5}\right) \\ & \times \left(\left(\frac{Time - 140}{100}\right) - 1.69\right) + \left(\frac{(KI - 0.5)}{0.5}\right) \\ & \times \left(\left(\frac{KI - 0.5}{0.5}\right) - 7.33\right) + \left(\frac{(Time - 140)}{100}\right) \\ & \times \left(\left(\frac{Time - 140}{100}\right) - 0.39\right) \end{aligned} \quad (2)$$

$$\begin{aligned} \textit{TPC degradation} = {} & 66.19 - 2.94 \times \left(\frac{(GO - 0.6)}{0.6}\right) + 2.05 \times \left(\frac{KI - 0.5}{0.5}\right) \\ & + 23.94 \times \left(\frac{(Time - 140)}{100}\right) + \left(\frac{(GO - 0.6)}{0.6}\right) \\ & \times \left(\left(\frac{KI - 0.5}{0.5}\right) - 4.68\right) + \left(\frac{(KI - 0.5)}{0.5}\right) \\ & \times \left(\left(\frac{Time - 140}{100}\right) - 8.55\right) + \left(\frac{(KI - 0.5)}{0.5}\right) \\ & \times \left(\left(\frac{KI - 0.5}{0.5}\right) - 6.55\right) + \left(\frac{(Time - 140)}{100}\right) \\ & \times \left(\left(\frac{Time - 140}{100}\right) - 11.07\right) \end{aligned} \quad (3)$$

The adequacy of the model was justified through ANOVA and the results are shown in Table 3. In this case, the low probability value for regression model equations (p-value = 0.0001 or less) indicates that the quadratic models fitted to the experimental results well. The lack-of-fit was calculated from the experimental error (pure error) and residuals. Prob > F higher than 0.05 in both models confirms a not significant lack of fit. Furthermore, the second-order polynomial models were highly significant for 95% confidence level due to having F-ratios of 104.03 and 118.23 for lignin and TPC degradation, respectively. The fitted model was further verified by the correlation coefficient (R^2). According to the ANOVA results (Table 3), R^2 were 0.983788 and 0.985708 respectively for lignin and TPC degradation. The adjusted correlation coefficients (adj. R^2) values were found to be 0.974331 and 0.977371 for lignin and TPC degradation, respectively, indicating that

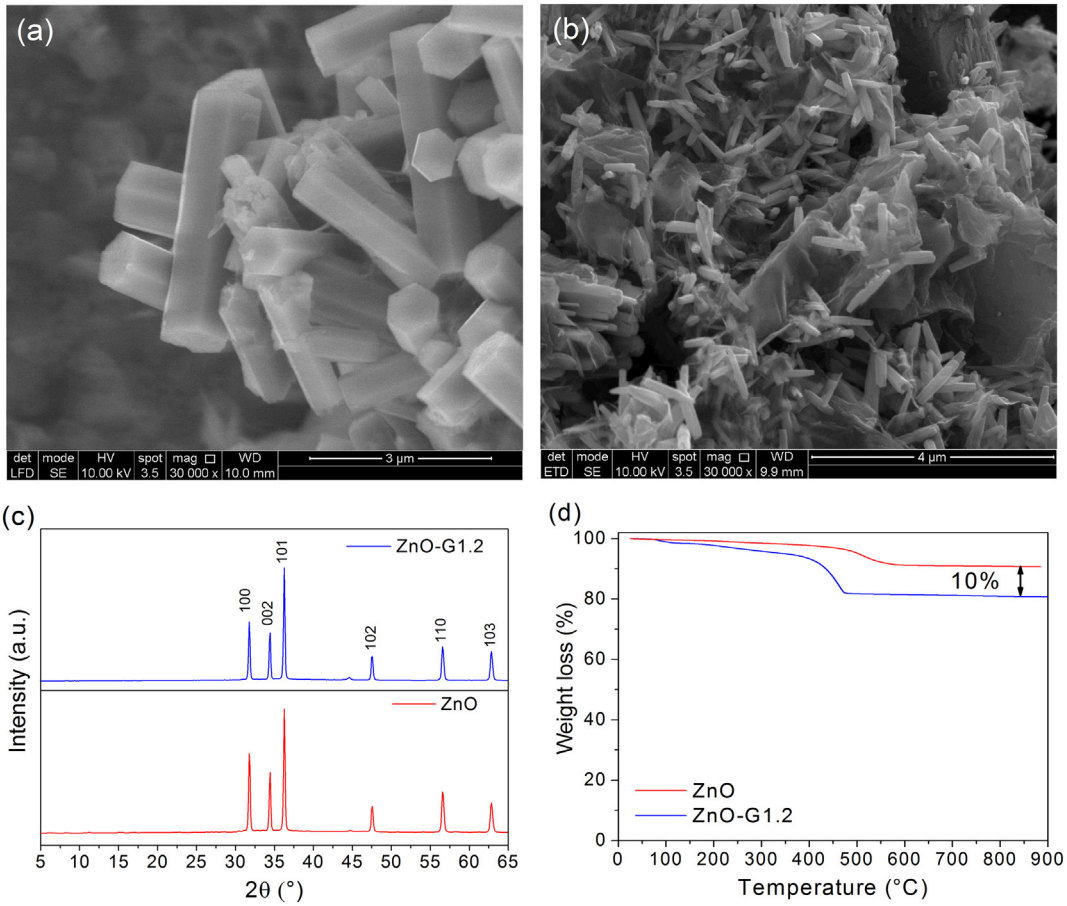

Fig. 1. SEM images of (a) ZnO and (b) ZnO-G1.2; (c) XRD spectra and (d) TGA curves of ZnO and ZnO-G1.2. The Raman scattering is an important technique to characterize electronic structure of carbonaceous materials, especially for distinguishing ordered and disordered crystal structures. The Raman spectra of GO and ZnO-G1.2 as presented in Fig. 2a had two prominent peaks at 1637 (G band) and 1382 cm^{-1} (D band). Generally the D band is representative as the disorder/defect band (Loryuenyong et al., 2013). For the D band, the results exhibited the current approach could effectively yield graphene with less defect nature. Furthermore, the increase in the peak intensity of the G band along with sharpening in the peak intensity in the composite is due to the restoring sp^2 domains and the reestablished sp^2 network upon the microwave treatment. After baseline correction, the intensity ratio of D and G band (I_D/I_G) of the composite was calculated to be 1.02, in which the slightly increase of I_D/I_G for GO suggested a reduction in the average size of sp^2 domains. This is in agreement with a former report (Zhou et al., 2012). The study of optical properties of ZnO and ZnO-G1.2 composite were probed with UV–vis diffuse reflectance spectroscopy and the resulting curves are shown in Fig. 2b. According to the spectra, both cases displayed an analogues pattern and a characteristic absorption sharp edge rising at 380 nm, indicating the same absorption and identical band gap energy which agrees well with the previous report (Liu et al., 2012). The energy band gap (E_g, eV) of samples was estimated to be about 3.26 eV from the onset of the absorption edge, according to the equation ($E_g = 1240/\lambda$) (Yang et al., 2014). However, the composite showed an extended photoresponsive range in the visible light region, suggesting a more efficient utilization of the wide spectrum of light as a consequence of the formation of interface between ZnO and graphene. Interestingly, an enhanced absorption in a visible light region is in agreement with the color change of ZnO-Gx samples (Fig. S1). The photocatalytic activity is intrinsically controlled by the electronic properties of semiconductor oxide, including the band gap and the band edge potential. However, on the basis of the band gap energy calculations, the graphene presence in ZnO did not result in any changes compared to the bare ZnO. It confirms that the photocatalytic activity improvement could not be directly ascribed to the band gap. To understand better the difference in the electronic properties of ZnO after hybridization with graphene sheet, XPS valence band spectra were recorded (Fig. 2c). As shown in Fig. 2c, ZnO had a deeper valence band maximum of 0.46 eV than ZnO-G1.2, indicating a stronger oxidation power of photoexcited valence band hole in the former. Based on the band gap calculated from Fig. 2b and valence band maximum determined from Fig. 2c, the relatively band positions in the absence and presence of graphene sheet (ZnO and ZnO-G1.2) *vs.* a normal hydrogen electrode (NHE, pH = 7) are shown in Fig. 2d. Based on the determined positon of valence band from Fig. 2d, ZnO possessed a suitable valence band position for water oxidation half-reaction by the photogenerated hole. However, the elevated valence band of ZnO-G1.2 had a positive potential (ca. +2.4 V *vs.* NHE); thus, the oxidation of water as possible electron donor ($H_2O/\cdot OH = +2.32$ V *vs.* NHE (Wood, 1988)) is expected to be thermodynamically difficult. It is interesting to note that both ZnO and ZnO-G1.2 could significantly generate $O_2\cdot^-$ radical during UV illumination since the conduction bond minimum is negative enough to contribute to the reduction of oxygen ($O_2/O_2\cdot^- = -0.33$ V *vs.* NHE (Wood, 1988)). These results are in agreement with previous report (Wang et al., 2013). This upward shift might be helpful during photocatalysis of phenolic compounds.

the obtained models were significant.

3.3. Response surface plotting for evaluation of operational parameters

The response surface graphs of lignin and TPC degradation in Fig. 3 are the graphical representation of the regression equations Eqs. (2) and (3) holding one variable at constant of it's zero level (GO = 0.6 mg/mL, KI = 0.5 mM, irradiation time = 140 min), while varying the other two variables within their experimental range.

The interaction effects of GO (x_1) and KI concentration (x_2) on the lignin and TPC degradation while keeping the value of irradiation time constant at zero level (*i.e.* 140 min) are shown in Fig. 3a and d, respectively. As shown in Fig. 3a, by increasing the KI concentration, the lignin degradation efficiency increased almost irrespectively of the GO content. It was found that the process reactivity became efficient when KI was used. This implies the necessity of adding KI for effective

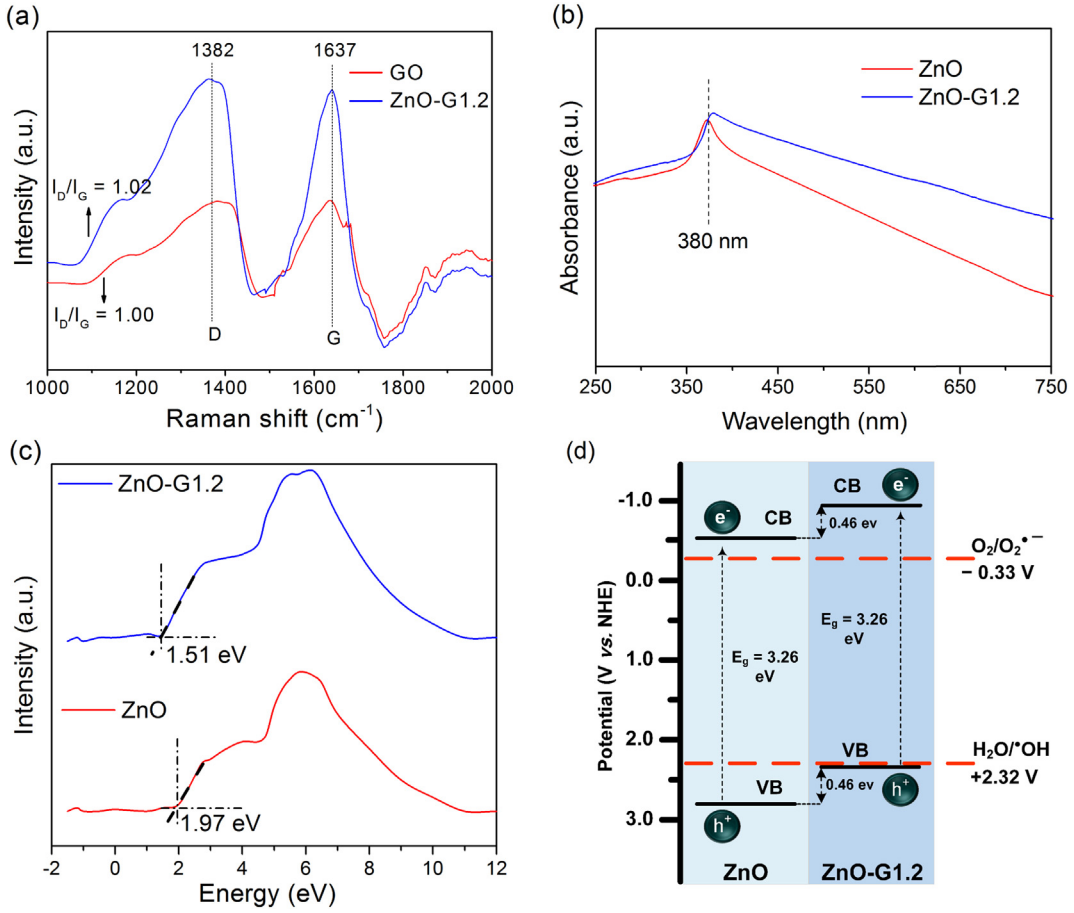

Fig. 2. (a) Raman spectra of bare GO and ZnO-G1.2; (b) UV–vis diffuse reflection spectra of ZnO and ZnO-G1.2; (c) XPS valence band spectra of ZnO and ZnO-G1.2, and (d) the determined valence and condition band edges of ZnO and ZnO-G1.2 (potentials are shown *versus* that of an NHE at pH = 7).

degradation of lignin in the photocatalytic system since this UV/Iodide/ZnO-Gx system can effectively take control of lignin degradation by the production of I·. Despite lignin degradation, TPC degradation efficiency was not only depended on the variation of KI concentration as shown in Fig. 3d. Importantly, the TPC degradation efficiency reached its minimum when the GO content into ZnO structure reached 1.2 mg/mL. This is desirable for preserving valuable phenolic compounds from oxidation without compromising the lignin degradation. It is worth mentioning that ZnO-G1.2 composite performed well showing degradation yield for TPC (55%) without addition any KI. This might be due to the fact that graphene sheets provide closer contact between phenolics and the composite by the π-π mechanism (Gaber et al., 2017; Wang et al., 2014). This mechanism as a prerequisite step results in concentrating the target organic pollutant around the composite surface, thus enhancing the efficiency of a photocatalytic reaction (Djurišić et al., 2014; Upadhyay et al., 2014). Furthermore, the CT complex (as addressed in the introduction) formed between iodide as the ED and photogenerated holes, accelerated the reactivity of the process with increasing KI concentration from 0 to 0.64 mM. However, it decreased when the concentration of KI further increased to 1 mM. The decrease of photocatalytic activity for KI concentration above 0.64 mM may be related to the ability of iodide ion to scavenge ·OH radicals when the excess amount of KI was added to the reaction system (Li et al., 2011), as shown in Eq. (4):

Table 3
ANOVA results for response surface quadratic models.

Responses	Source	Analysis of variance				
		Sum of square	df	Mean square	*F*-ratio	Prob > *F*
Lignin degradation	Model	4321.84	7	617.41	104.03	<0.0001
	Pure error	13.41	5	2.68		
	Lack of fit	57.81	7	8.26	3.08	0.1170
	C. Total	4393.06	19			
	R-squared	0.983788				
	Adj. R-squared	0.974331				
TPC degradation	Model	3204.05	7	457.72	118.23	0.0001
	Pure error	16.70	5	3.34		
	Lack of fit	29.76	7	4.25	1.27	0.41
	C. Total	3250.50	19			
	R-squared	0.985708				
	Adj. R-squared	0.977371				

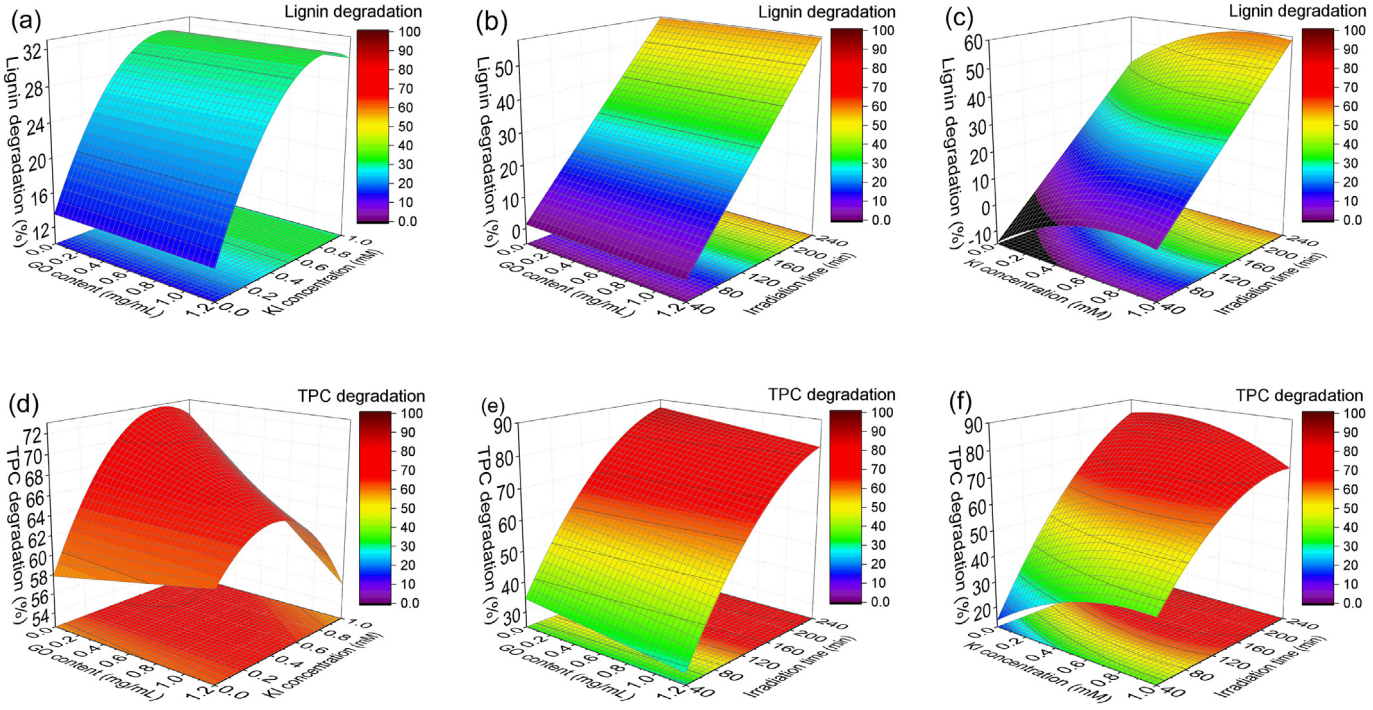

Fig. 3. Surface plots for degradation yield as a function of: GO and KI concentration at irradiation time of 140 min (lignin (a) and TPC (d)); GO and irradiation time at KI concentration of 0.5 mM (lignin (b) and TPC (e)); KI concentration and irradiation time at GO content of 0.6 mg/mL (lignin (c) and TPC (f)). [Fixed experimental conditions: [NaOH] = 25 mM; photocatalyst dosage 0.05 g/L; lignin concentration 0.1 g/L].

$$I^- + OH \rightarrow I^{\cdot} + OH^- \quad (4)$$

The effects of GO (x_1) and irradiation time (x_3) on the degradation of lignin and TPC are demonstrated in Fig. 3b and e. The KI concentration was fixed at 0.5 mM. As illustrated in Fig. 3b, the photocatalytic lignin degradation was found to increase with the increase of time, irrespective of the change in GO. The highest lignin degradation increased with further increasing time reaching the highest value of 63.20% after 240 min irradiation. However, the photocatalytic degradation of TPC as shown in Fig. 3e had a rapid increase at the beginning of the experiment, and then with further increasing time, no changes occurred in the reactivity. The degradation yield was observed to reach rapidly equilibrium within shorter timeframes by approximately 75% efficiency after 180 min. Similar to lignin degradation, the changing in GO content seemed to have no effect on the TPC yield compared to that of time. It can be concluded that the degradation of lignin is more favorable compared to the TPC degradation over longer irradiation time *via* UV/Iodide/ZnO-Gx process.

Fig. 3c and f present the effect of KI concentration (x_2) and irradiation time (x_3) on the degradation of lignin and TPC, respectively. The GO content was kept constant at 0.6 mg/mL. The lignin degradation increases continuously with an increase of KI concentration and irradiation time. Specifically, it was found that the process showed higher lignin degradation at high irradiation time and the maximum degradation of 62% was obtained when the concentration of KI solution was 0.8 mM. However, the different trend is obtained for TPC degradation as can be seen in Fig. 3f. Clearly, it is obvious that TPC degradation reaches a maximum at the region in the KI concentration range of 0 to 0.6 mM and prolonged irradiation time, in which no further degradation seemed occur. For KI concentration higher than 0.6 mM, the TPC degradation at a constant value of 0.6 mg/mL GO content was inclined to decrease. However, this decrement was not as high as the significant drop achieved in the TPC degradation by 1.2 mg/mL GO content as discussed in Fig. 3d.

3.4. Process optimization

At the optimum conditions, lignin decomposes and TPC preserves to exploit a chemically valuable solution (*i.e.* less lignin and high TPC) and biological available solid residue (*i.e.* comprising less lignin compartment) for further usages. To this end, optimization of the input space by RSM approach is obtained with a degradation yield as high as 52% for lignin and 55% for TPC at the conditions as follows: KI concentration = 0.64 mM; GO content 1.2 mg/mL; 240 min of irradiation time. The adequacy of predicted experimental results was checked by carrying out three replicative experiments under the optimal conditions. The average values corresponding to the objective goals are 50.12% for lignin and 54.84% for TPC. The good agreement between the predictive results and experimental results validates the optimal conditions. Phenolics produced in optimized conditions were qualified with the GC/MS instrument. Fig. S3 depicts the GC/MS total ion chromatograms of phenolics obtained after photocatalysis of lignin at optimized conditions. It is evident that main reaction products detected were 2-methoxy-phenol (retention time: 12.80 min, major ions: 124, 109, 81) and 2-ethyl-phenol (retention time: 14.95 min, major ions: 122, 107, 77) with a number of other intermediates at concentrations lower than the detectable limit. After 60 min of exposure to UV/TiO_2 system, it was found that the derived compounds from organosolv pulping black liquors were syringaldehyde, pyrocatechol, raspberry ketone, and vanillin (Prado et al., 2013). Guaiacol yield (%) reached to 8.7% by using TiO_2 under solar light irradiation by using sodium of lignosulfonate lignin type (Gong et al., 2017). The overall mass conversion of lignin to organic compounds in the total time period including dark stirring and photocatalysis was found to be in the range of 17–20 wt% for TiO_2–lignin mixtures obtained by wet milling in presence of water. In this case, maximum production of ethyl benzene (≈150 mg/g) was observed at 1 h of irradiation. Vanillin and acetyl vanillin production (< 5 mg/g) decreased along with UV irradiation. Syringaldehyde and acetosyringone production continuously increased with extension of irradiation time period reaching the highest value of 10 mg/g for both of them (Nair et al., 2016).

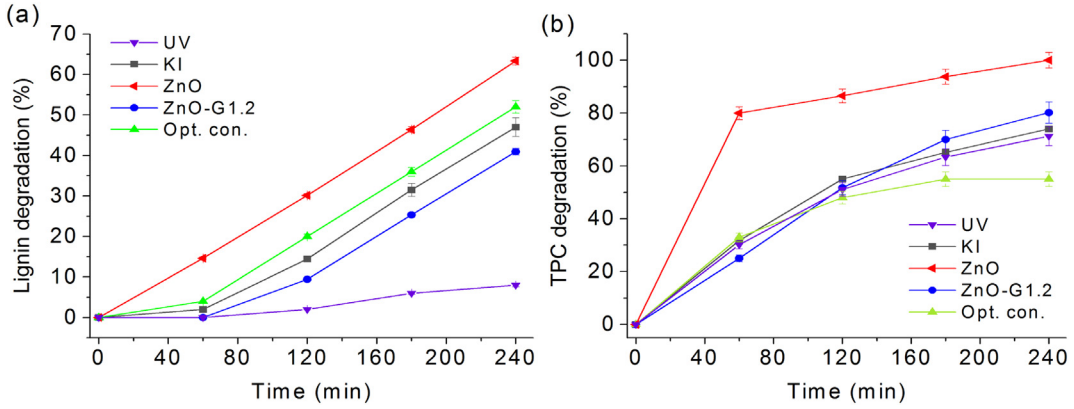

Fig. 4. (a) Lignin and (b) TPC degradation at different conditions as function of time: [KI] = 0.64 mM, ZnO and ZnO-G1.2 of 0.05 g/L, the optimized conditions including [KI] = 0.64 mM and ZnO-G1.2 of 0.05 g/L. Other conditions: lignin concentration 0.1 g/L, [NaOH] = 25 mM, air purging.

3.5. Photocatalytic mechanism

To elucidate the photodegradation mechanism of lignin and TPC at the optimized conditions, comparative photocatalytic experiments were carried out. For comparison, UV, KI, ZnO, and ZnO-G1.2 were separately added as a reference at each optimized value to understand the way that affected the process.

As can be seen from Fig. 4a, during UV illumination period, no appreciable increase in lignin degradation in the aqueous phase could be observed. This is in agreement with the previous reports where they concluded that direct photolysis of lignin is negligible (Kansal et al., 2008; Kobatakawa et al., 1989). As observed, pure ZnO alone had no selectivity towards lignin degradation with 62% yield. This efficiency is attributed to the ability of UV/ZnO system to produce ·OH radicals by oxidation of hydroxyl at its valence band (Yang et al., 2015; Zhang et al., 2018). Previously, it has been reported that the attraction of ·OH radicals on the double bonds in the aromatic ring is the major mechanism of lignin oxidization (H. Li et al., 2015; MacHado et al., 2000; Makhotkina et al., 2008; Nair et al., 2016). In the absence of KI, UV/ZnO-G1.2 system seemed to be ineffective for lignin degradation by having the value of 38%. As it mentioned, the band shift of ZnO-G1.2 to more reducing potential, in principle may affect the production of ·OH radicals. In aerated system, molecular oxygen acts as an efficient electron scavenger to capture the electron to form superoxide anion radical ($O_2\cdot^-$) (Song et al., 2007). In our system, $O_2\cdot^-$ was readily generated from oxygen by trapping the photoinduced electrons from both photocatalysis and CTTS mechanism of iodide photolysis. However, the production of $O_2\cdot^-$ seemed to be less impact on direct oxidation of lignin owing to its low redox potential (0.89 V, *vs.* NHE) compared to ·OH radicals with high redox potential (2.8 V, *vs.* NHE) (Gong et al., 2017). Based on the above discussion, we should expect lower degradation yield for the ZnO-G1.2 system compared to pure ZnO. With respect to KI alone system, KI was found to provide a strong condition for degradation of lignin *via* production of I·. This suggests the importance of using KI in assistance with photocatalysis in order to enhance lignin degradation. To this end, degradation efficiency boosted significantly to more than the yield of the ZnO-G1.2 system when tests were conducted at UV/KI/ZnO-G1.2 system.

The photocatalytic activity for phenolic degradation can be evaluated *via* comparing the apparent rate constant (k_{app}, min^{-1}) of pseudo-first-order reaction, as it widely used in photocatalytic degradation of phenol (Hosseini et al., 2018; Saratale et al., 2014; Tryba et al., 2006). The k_{app} can be calculated from the slope of ln (C_0/C_t) *vs.* time, where C_0 and C_t are the concentration of phenol (mg/L) when the irradiation time is 0 and t, respectively. The obtained values of k_{app} are listed in Table S1 and the fitted model to the experimental data is represented in Fig. S2. As can be seen, the values of k_{app} followed the order: ZnO composite (0.0164 min^{-1}), ZnO-G1.2 (0.0066 min^{-1}), KI (0.0058 min^{-1}), bare UV (0.0054 min^{-1}), and optimized condition (0.0041 min^{-1}).

Fig. 4b shows the photocatalytic degradation of phenolics. On the contrary to lignin photolysis, it was found that the pronounced increase in TPC photolysis occurred in the above-mentioned condition (*i.e.* lignin dosage 0.1 g/L; photocatalyst dosage 0 g/L; [NaOH] = 25 mM) (Fig. 4b). This could be due to the fact that CTTS mechanism of phenolics - in the absence of photocatalyst upon UV illumination - follows by transformation of phenol to phenoxyl radical ($C_6H_5O\cdot$) and production of $e_{aq}-$ at pH above 12 (Gu et al., 2017). Furthermore, this CTTS also can contribute to the production of more $O_2\cdot^-$ radicals alongside with that of iodide photolysis. $O_2\cdot^-$ is expected to result in the selective oxidation of phenolics owing to suitable oxidation potential with longer lifetime as its advantages over ·OH (MacHado et al., 2000). Notably, there was no difference observed for TPC degradation between UV (0.0054 min^{-1}) and UV/KI (0.0058 min^{-1}) process, suggesting no effect of KI against phenolics. It should be noted that UV/Iodide system has specific features to contribute to the reaction *via* similar way of phenolics by ejecting $e_{aq}-$ into solution *via* CTTS states (Lehr et al., 1999) on a femtosecond time scale. However, CTTS mechanism of iodide had no effect on the yield of phenolics because CTTS of phenolics itself is expected to occure on a picosecond time scale (Mialocq et al., 1980) which is extremely faster than that of KI. According to Fig. 4b, for ZnO, the close to 100% TPC degradation efficiency with k_{app} value of 0.0164 min^{-1} suggests that the produced radicals including ·OH and $O_2\cdot^-$ on the surface of ZnO are sufficient for complete degradation of phenolic compounds. Furthermore, when graphene is introduced into pure ZnO, the degradation yield for TPC dropped sharply. This could be due to the upward shift towards relative energy band gap, leaving maximum valence band in the composite with less oxidation power, which makes it unable to produce highly enough non selective ·OH radicals. In addition, the value of k_{app} for the composite decreases by the factor of 2.48, compared with that of pure ZnO. When the optimized condition was tried, the k_{app} reduced by the factor of 4 with regard to that of pure ZnO. Increased selectivity towards TPC may be attributed to the fact that at the optimized conditions KI had already scavenged the hole *via* CT mechanism, inhibiting the production of ·OH from the oxidation of water in the photogenerated hole of the composite, as shown in Eq. (7). Another possible explanation for inhibiting the production of ·OH might be due to the fact that iodide reacts directly with ·OH, as described by Eq. (4) (Li et al., 2011). When the generation of ·OH significantly is inhibited, it can eventually minimize the decomposition of phenolics, since this radical is major active species reported for phenolic degradation (Ahmed et al., 2010). Furthermore, the $e_{aq}-$ produced during photolysis of iodide and phenolics could be ejected to the graphene sheet due to its conductivity and

tremendous mobility for shuttling and storage of electron (Zhang et al., 2013). Therefore, graphene sheet can increase the lifetime of electron, producing more $O_2\cdot^-$ radicals.

Based on above explanations, the following mechanism was proposed for UV/KI/ZnO-G1.2 system. The photoinduced electrons were generated from photocatalysis and photolysis process through the multistep continuous reactions, as described in Eqs. (5) and (9). These separated electrons would subsequently eject on the surface of graphene sheets, ready for quenching by O_2 to form $O_2\cdot^-$ by Eqs. (6) and (9). Furthermore, excess amount of ·OH may be scavenged by the extra amount of iodide added to the reaction medium (Eq. (10)). Above results indicate that the enhancement in the selective oxidation of lignin due to graphene and KI addition may be attributed to the higher production of $O_2\cdot^-$ accompanying by the lower generation of ·OH in UV/KI/ZnO-G1.2 system.

$$ZnO - G1.2 + h\nu \rightarrow e^- + h^+ \quad (5)$$

$$e^-(ZnO - G1.2) + O_2 \rightarrow O_2^- \quad (6)$$

$$6h^+(ZnO - G1.2) + I^- + 6OH^- \rightarrow IO_3^- + 3H_2O \quad (7)$$

$$h^+(ZnO - G1.2) + OH^- \rightarrow \cdot OH \quad (8)$$

$$e_{aq}^-(CTTS\ meachanism) + O_2 \rightarrow O_2^- \quad (9)$$

$$I^- + \cdot OH \rightarrow I\cdot + OH^- \quad (10)$$

To further support the hypothesis for inhibition of ·OH generation in the composite, the PL technique was employed to detect qualitatively the ·OH formed on the surfaces of photocatalysts along with different conditions. For comparison, the concentration of KI at the optimized conditions was also tested as a reference. Fig. 5 shows the fluorescence spectral changes observed during light irradiation of ZnO and ZnO-G1.2 in a basic terephthalic acid (TA) solution (excitation wavelength at 315 nm) originated from the formation of a highly fluorescent product of 2-hydroxyterephtahalic acid (TAOH) by reaction with ·OH. As shown, the PL intensity around 425 nm profoundly changed at different conditions, which demonstrates the production of the ·OH. It is worthy to mention that production of ·OH decreased from ZnO to ZnO-G1.2 as the valence band maximum at ZnO-G1.2 shift upward to lower oxidation potential. In addition, in the case of KI and optimized conditions, no photo-fluorescence generation was observed, indicating no ·OH was formed during both conditions. These results confirm again our hypothesis for retardation of ·OH generation when the optimized conditions tried.

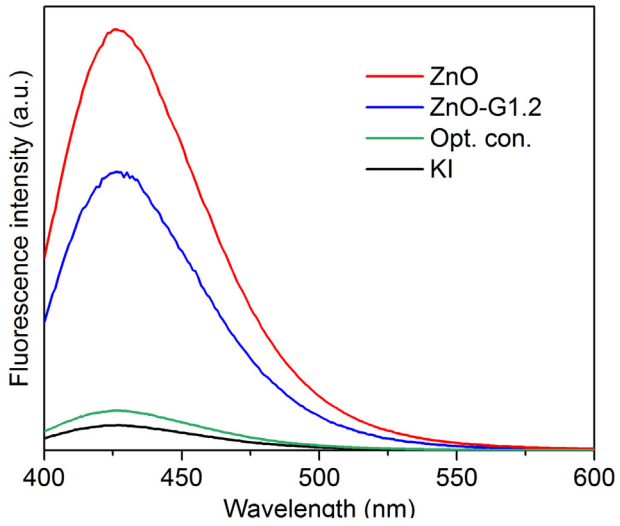

Fig. 5. ·OH radical qualification with terephthalic acid 0.5 mM and 2 mM NaOH at different conditions: [KI] = 0.64 mM, ZnO and ZnO-G1.2 of 0.05 g/L, the optimized conditions including: [KI] = 0.64 mM and ZnO-G1.2 of 0.05 g/L.

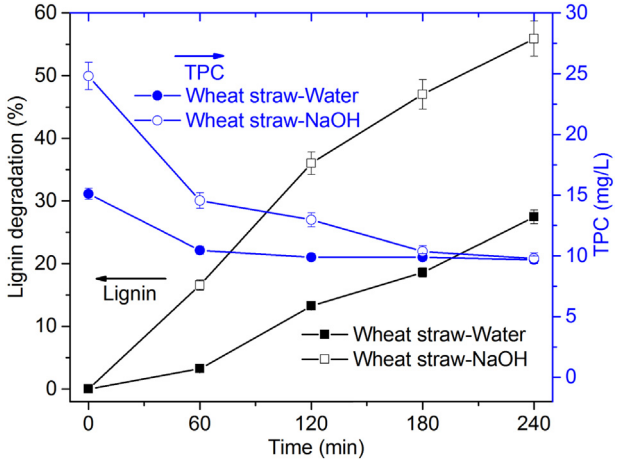

Fig. 6. Lignin and TPC degradation in UV/KI/ZnO-G1.2 system; (ZnO-G1.2 dosage 0.05 g/L, wheat straw concentration 1 g/L, [NaOH] = 25 mM, [KI] = 0.64 mM).

3.6. Effect of photocatalytic pretreatment on biomass structural changes and anaerobic biodegradability

To evaluate the applicability of the process at the optimized conditions, lignin was replaced by wheat straw as a real biomass. The experiments were performed with increasing the loading of straw to 1 g/L to investigate the phenolic and lignin degradation with two different ways of water and NaOH soaking. As can be seen in Fig. 6, lignin degradation increased over photocatalysis time. This trend was more pronounced in case of lignin soaked into alkaline medium, compared to water-soaked straw. These results are in line with previous reports in which they manifested better photocatalytic lignin degradation in alkaline medium compared to the neutral and acidic conditions (H. Li et al., 2015; Kansal et al., 2008; Tsapekos et al., 2018). TPC also showed the sharp decrease in the first hour of irradiation. However, there was no observable change occurred beyond the first hour. This might be due to the possible interaction between the π system of graphene and the π unit of phenolics. In this sense, it could be assumed the strong π interaction may act as poison on the surface area of composite, limiting of active photocatalytic surface area (Ajmal et al., 2014). As shown for straw soaked into water, there was no significant change of TPC during photocatalysis, which implies the importance of using NaOH. The reason for strong photocatalysis might be attributed to the fact that at alkaline conditions the stage of lignin precipitation could be bypassed as lignin is better dissolved and thus, the diffusion of the reactant to the photocatalyst surface, where the localized oxidants are present, is facilitated. This condition also facilitates the production of low molecular weight phenolic fragments (Evstigneev, 2011; Nair et al., 2016; Tsapekos et al., 2018). Interestingly, for both water and NaOH straw soaked samples, experiments conducted at the optimized conditions showed similar trend with that of lignin samples in which the TPC degradation reached a constant value at longer times.

Different straw samples were characterized by FTIR spectroscopy to investigate the change in the main functional groups and chemical structure of the untreated and pretreated solid residues. As shown in Fig. 7, all wheat straw samples showed similar characteristic bonds at 3332, 2920, 1585, 1420, 1030, and 877 cm^{-1} corresponding to O—H stretching in hydroxyl group (Kang et al., 2018), C—H stretching in methyl and methylene groups (Niu et al., 2009), carbonyl groups conjugated with an aromatic ring (Xu et al., 2013), aromatic skeletal vibrations combined with C—H in-plane deformation (Kumirska et al., 2010), C—O—H stretching of primary and secondary alcohols (Kumirska et al., 2010), C—O—C stretching of β-glycosidic bonds (Feng Xu et al., 2013; Kumirska et al., 2010), respectively. A comparison between the

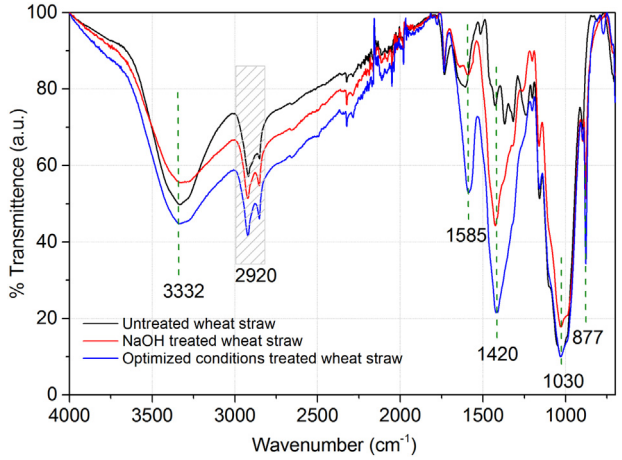

Fig. 7. FTIR spectra (vector-normalized and baseline-corrected) of straw samples before and after pretreatment.

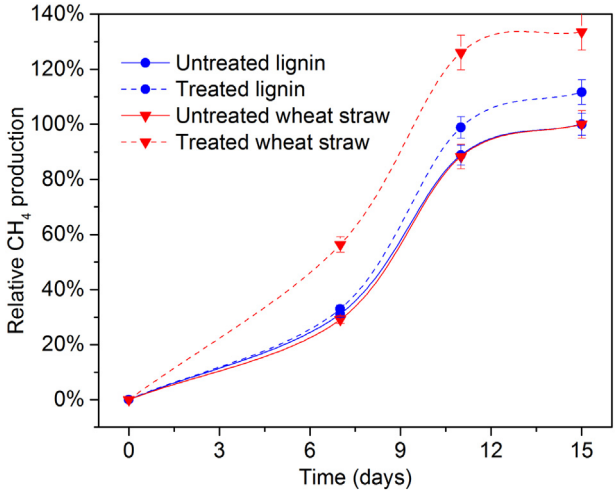

Fig. 9. Relative CH_4 production of untreated and treated lignin and wheat straw.

untreated and treated wheat straw shows that the bands are rather similar and so, the chemical structures are relatively equal. Very strong vibrations were detected for aromatic skeleton vibrations ranging 1600–1400 cm^{-1}, indicating for changes in aromatic substitutions and formation of new non-conjugated intermediate compounds in wheat straw treated at optimized conditions compared to NaOH and untreated one. The increase of intensity at this range was also observed during photocatalytic alkali lignin degradation with rare earth doped titanium dioxide (Song et al., 2015).

The SEM images of wheat straw after and before photocatalysis at the optimized conditions were used to present the structural change occurred during treatment in the (Fig. 8). As can be seen from the SEM image of NaOH treated straw (Fig. 8a), the material surface seemed to remain intact, compact and inaccessible for microbial activity, suggesting the need for pretreatment. From Fig. 8b, it can be seen that after photocatalytic treatment, straw underwent significant structural change, especially in terms of the surface where the lignin layer (outer layer) protects the structure from any rupture. The obtained structure of straw found to be opened-up which facilitates the easy access of microorganisms to lignocellulosic biomass compared to the rigid structure shown in Fig. 8a.

Due to the increased efficiency observed at alkaline condition, a set of biodegradability experiments was carried out for both straw and lignin soaked with NaOH to examine the potential of using the photocatalytically pretreated biomass and lignin for biogas production. For both treated samples, higher methane production was observed compared to their corresponding untreated samples (Fig. 9). Specifically, treated wheat straw at optimized conditions resulted 35% increment compared to untreated one. This result is comparable to a previous study in which treatment of wheat straw with pure titanium dioxide showed enhancement up to 37% in biogas production compared to untreated sample (Alvarado-Morales et al., 2017). The results from monitoring the methane production suggested that the disrupted lignocellulosic matrix was more easily available to the anaerobic digestion microbiome that in turn favored the bioenergy yield.

4. Conclusion

UV/Iodide/ZnO-G process exhibited selective photocatalytic activity for lignin degradation due to the presence of graphene and KI. As a result, the production of ·OH, which is responsible for degradation of phenolics, becomes restricted. The quadratic equation of RSM was optimized to achieve maximum yield of lignin degradation and minimum yield of TPC degradation. In this regard, degradation yield as high as 52% for lignin and 55% for TPC at the conditions as follows: [KI] = 0.64 mM; GO content 1.2 mg/mL; 240 min of irradiation time, was achieved. Wheat straw pretreatment at the optimal conditions resulted in 58% lignin degradation yield. Treated wheat straw at optimized conditions also shown in 35% increment in methane production

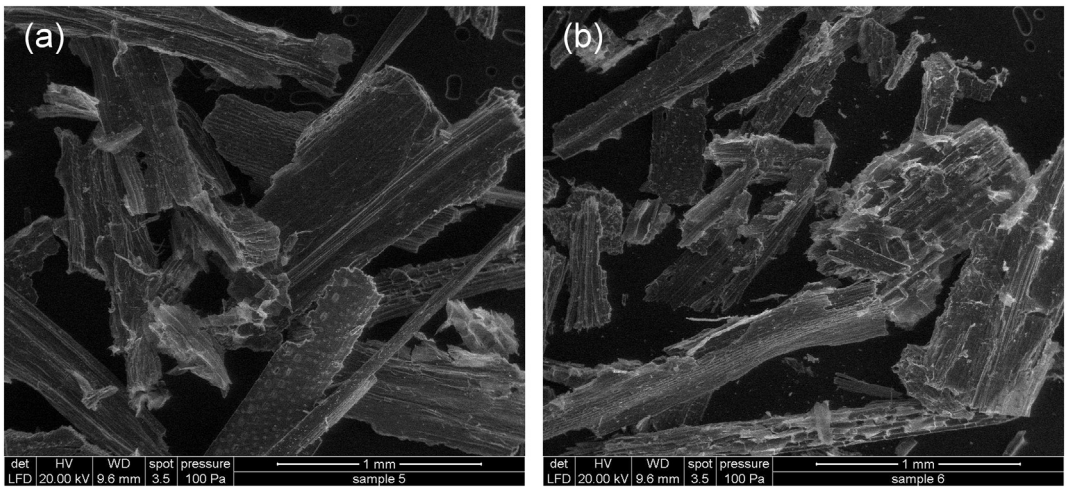

Fig. 8. SEM images of (a) NaOH treated wheat straw and (b) wheat straw treated at the optimized conditions.

compared to untreated one. FTIR and SEM analysis were successfully supported the fact that bioavailability of lignocellulosic materials increased with disruption of lignin compartment in the solid phase of wheat straw. Overall, this novel strategy can play a key role in the conversion of lignin into valuable phenolics and increased biogas production.

Conflicts of interest

There are no conflicts to declare.

Funding sources

This research did not receive any specific grant from funding agencies in the public, commercial, or not-for-profit sectors.

Acknowledgments

The authors thank Hector Garcia for technical assistance.

Appendix A. Supplementary data

Supplementary data to this article can be found online at https://doi.org/10.1016/j.envint.2018.12.062.

References

Ahmed, S., Rasul, M.G., Martens, W.N., Brown, R., Hashib, M.A., 2010. Heterogeneous photocatalytic degradation of phenols in wastewater: a review on current status and developments. Desalination. https://doi.org/10.1016/j.desal.2010.04.062.

Ainsworth, E.A., Gillespie, K.M., 2007. Estimation of total phenolic content and other oxidation substrates in plant tissues using Folin-Ciocalteu reagent. Nat. Protoc. 2, 875–877. https://doi.org/10.1038/nprot.2007.102.

Ajmal, A., Majeed, I., Malik, N., 2014. Principles and mechanisms of photocatalytic dye degradation on TiO_2 based photocatalysts: a comparative overview. RSC Adv. 4, 37003–37026. https://doi.org/10.1039/C4RA06658H.

Al-Hamdi, A.M., Sillanpää, M., Dutta, J., 2015. Photocatalytic degradation of phenol by iodine doped tin oxide nanoparticles under UV and sunlight irradiation. J. Alloys Compd. 618, 366–371. https://doi.org/10.1016/j.jallcom.2014.08.120.

Alvarado-Morales, M., Tsapekos, P., Awais, M., Gulfraz, M., Angelidaki, I., 2017. TiO_2/UV based photocatalytic pretreatment of wheat straw for biogas production. Anaerobe 46, 155–161. https://doi.org/10.1016/j.anaerobe.2016.11.002.

Angelidaki, I., Alves, M., Bolzonella, D., Borzacconi, L., Campos, J.L., Guwy, A.J., Kalyuzhnyi, S., Jenicek, P., Van Lier, J.B., 2009. Defining the biomethane potential (BMP) of solid organic wastes and energy crops: a proposed protocol for batch assays. Water Sci. Technol. 59, 927–934. https://doi.org/10.2166/wst.2009.040.

Awungacha Lekelefac, C., Busse, N., Herrenbauer, M., Czermak, P., 2015. Photocatalytic based degradation processes of lignin derivatives. Int. J. Photoenergy 2015.

Chen, J., Liu, W., Song, Z., Wang, H., Xie, Y., 2018. Photocatalytic degradation of β-O-4 lignin model compound by In2S3 nanoparticles under visible light irradiation. Bioenergy Res. 11, 166–173. https://doi.org/10.1007/s12155-017-9886-8.

Den, W., Sharma, V.K., Lee, M., Nadadur, G., Varma, R.S., 2018. Lignocellulosic biomass transformations via greener oxidative pretreatment processes: access to energy and value-added chemicals. Front. Chem. 6. https://doi.org/10.3389/fchem.2018.00141.

Djurišić, A.B., Leung, Y.H., Ching Ng, A.M., 2014. Strategies for improving the efficiency of semiconductor metal oxide photocatalysis. Mater. Horiz. 1, 400–410. https://doi.org/10.1039/c4mh00031e.

Evstigneev, E.I., 2011. Factors affecting lignin solubility. Russ. J. Appl. Chem. 84, 1040–1045. https://doi.org/10.1134/S1070427211060243.

Fan, H., Zhao, X., Yang, J., Shan, X., Yang, L., Zhang, Y., Li, X., Gao, M., 2012. ZnO-graphene composite for photocatalytic degradation of methylene blue dye. Catal. Commun. 29, 29–34. https://doi.org/10.1016/j.catcom.2012.09.013.

Felício, C.M., Machado, A.E. da H., Castellan, A., Nourmamode, A., Perez, D. da S., Ruggiero, R., 2003. Routes of degradation of β-O-4 syringyl and guaiacyl lignin model compounds during photobleaching processes. J. Photochem. Photobiol. A Chem. 156, 253–265. https://doi.org/10.1016/S1010-6030(03)00007-8.

Gaber, D., Abu Haija, M., Eskhan, A., Banat, F., 2017. Graphene as an efficient and reusable adsorbent compared to activated carbons for the removal of phenol from aqueous solutions. Water Air Soil Pollut. 228, 320. https://doi.org/10.1007/s11270-017-3499-x.

Gong, J., Imbault, A., Farnood, R., 2017. The promoting role of bismuth for the enhanced photocatalytic oxidation of lignin on Pt-TiO_2 under solar light illumination. Appl. Catal. B Environ. 204, 296–303. https://doi.org/10.1016/j.apcatb.2016.11.045.

Gouvêa, C.A.K., Wypych, F., Moraes, S.G., Durán, N., Peralta-Zamora, P., 2000. Semiconductor-assisted photodegradation of lignin, dye, and kraft effluent by Ag-doped ZnO. Chemosphere 40, 427–432. https://doi.org/10.1016/S0045-6535(99)00312-4.

Gu, J., Ma, J., Jiang, J., Yang, L., Yang, J., Zhang, J., Chi, H., Song, Y., Sun, S., Tian, W.Q., 2017. Hydrated electron (eaq−) generation from phenol/UV: efficiency, influencing factors, and mechanism. Appl. Catal. B Environ. 200, 585–593. https://doi.org/10.1016/j.apcatb.2016.07.034.

Hansen, K.M.S., Zortea, R., Piketty, A., Rodriguez, S., Rasmus, H., 2013. Photolytic removal of DBPs by medium pressure UV in swimming pool water. Sci. Total Environ. 443, 850–856. https://doi.org/10.1016/j.scitotenv.2012.11.064.

Hosseinabadi-Farahani, Z., Hosseini-Monfared, H., Mahmoodi, N.M., 2015. Graphene oxide nanosheet: preparation and dye removal from binary system colored wastewater. Desalin. Water Treat. 56, 2382–2394. https://doi.org/10.1080/19443994.2014.960462.

Hosseini, F., Kasaeian, A., Pourfayaz, F., Sheikhpour, M., Wen, D., 2018. Novel ZnO-Ag/MWCNT nanocomposite for the photocatalytic degradation of phenol. Mater. Sci. Semicond. Process. 83, 175–185. https://doi.org/10.1016/j.mssp.2018.04.042.

Jimenez-Relinque, E., Castellote, M., 2015. Quantification of hydroxyl radicals on cementitious materials by fluorescence spectrophotometry as a method to assess the photocatalytic activity. Cem. Concr. Res. 74, 108–115. https://doi.org/10.1016/j.cemconres.2015.04.011.

Julkapli, N.M., Bagheri, S., 2015. Graphene supported heterogeneous catalysts: an overview. Int. J. Hydrog. Energy 40, 948–979. https://doi.org/10.1016/j.ijhydene.2014.10.129.

Kang, X., Sun, Y., Li, L., Kong, X., Yuan, Z., 2018. Improving methane production from anaerobic digestion of Pennisetum Hybrid by alkaline pretreatment. Bioresour. Technol. 255, 205–212. https://doi.org/10.1016/j.biortech.2017.12.001.

Kansal, S.K., Singh, M., Sud, D., 2008. Studies on TiO_2/ZnO photocatalysed degradation of lignin. J. Hazard. Mater. 153, 412–417. https://doi.org/10.1016/j.jhazmat.2007.08.091.

Khoshnevisan, B., Tsapekos, P., Alvarado-Morales, M., Angelidaki, I., 2018. Process performance and modelling of anaerobic digestion using source-sorted organic household waste. Bioresour. Technol. 247, 486–495. https://doi.org/10.1016/j.biortech.2017.09.122.

Kobatakawa, K., Sato, Y., Nakamura, S., Fujishima, A., 1989. Photodecomposition of kraft lignin catalyzed by TiO_2. Bull. Chem. Soc. Jpn. 62, 3433–3436. https://doi.org/10.1246/bcsj.62.3433.

Kou, J., Lu, C., Wang, J., Chen, Y., Xu, Z., Varma, R.S., 2017. Selectivity enhancement in heterogeneous photocatalytic transformations. Chem. Rev. 117, 1445–1514. https://doi.org/10.1021/acs.chemrev.6b00396.

Kumar, V., Kim, K.H., Park, J.W., Hong, J., Kumar, S., 2017. Graphene and its nanocomposites as a platform for environmental applications. Chem. Eng. J. 315, 210–232. https://doi.org/10.1016/j.cej.2017.01.008.

Kumirska, J., Czerwicka, M., Kaczyński, Z., Bychowska, A., Brzozowski, K., Thöming, J., Stepnowski, P., 2010. Application of spectroscopic methods for structural analysis of chitin and chitosan. Mar. Drugs 8, 1567–1636. https://doi.org/10.3390/md8051567.

Lehr, L., Zanni, M.T., Frischkorn, C., Weinkauf, R., Neumark, D.M., 1999. Electron solvation in finite systems: femtosecond dynamics of iodide·(water)(n) anion clusters. Science 284 (80), 635–638. https://doi.org/10.1126/science.284.5414.635.

Li, Y., Wang, J., Yao, H., Dang, L., Li, Z., 2011. Efficient decomposition of organic compounds and reaction mechanism with BiOI photocatalyst under visible light irradiation. J. Mol. Catal. A Chem. 334, 116–122. https://doi.org/10.1016/j.molcata.2010.11.005.

Li, B., Liu, T., Wang, Y., Wang, Z., 2012. ZnO/graphene-oxide nanocomposite with remarkably enhanced visible-light-driven photocatalytic performance. J. Colloid Interface Sci. 377, 114–121. https://doi.org/10.1016/j.jcis.2012.03.060.

Li, H., Lei, Z., Liu, C., Zhang, Z., Lu, B., 2015a. Photocatalytic degradation of lignin on synthesized Ag-AgCl/ZnO nanorods under solar light and preliminary trials for methane fermentation. Bioresour. Technol. 175, 494–501. https://doi.org/10.1016/j.biortech.2014.10.143.

Li, Y., Qu, J., Gao, F., Lv, S., Shi, L., He, C., Sun, J., 2015b. In situ fabrication of Mn_3O_4 decorated graphene oxide as a synergistic catalyst for degradation of methylene blue. Appl. Catal. B Environ. 162, 268–274. https://doi.org/10.1016/j.apcatb.2014.06.058.

Liu, X., Pan, L., Zhao, Q., Lv, T., Zhu, G., Chen, T., Lu, T., Sun, Z., Sun, C., 2012. UV-assisted photocatalytic synthesis of ZnO-reduced graphene oxide composites with enhanced photocatalytic activity in reduction of Cr(VI). Chem. Eng. J. 183, 238–243. https://doi.org/10.1016/j.cej.2011.12.068.

Liu, X., Zhao, L., Lai, H., Li, S., Yi, Z., 2017. Efficient photocatalytic degradation of 4-nitrophenol over graphene modified TiO_2. J. Chem. Technol. Biotechnol. 92, 2417–2424. https://doi.org/10.1002/jctb.5251.

Loryuenyong, V., Totepvimarn, K., Eimburanapravat, P., Boonchompoo, W., Buasri, A., 2013. Preparation and characterization of reduced graphene oxide sheets via water-based exfoliation and reduction methods. Adv. Mater. Sci. Eng. 2013. https://doi.org/10.1155/2013/923403.

Lu, Y., Wei, X.-Y., Wen, Z., Chen, H.-B., Lu, Y.-C., Zong, Z.-M., Cao, J.-P., Qi, S.-C., Wang, S.-Z., Yu, L.-C., Zhao, W., Fan, X., Zhao, Y.-P., 2014. Photocatalytic depolymerization of rice husk over TiO_2 with H_2O_2. Fuel Process. Technol. 117, 8–16. https://doi.org/10.1016/J.FUPROC.2013.04.001.

Ma, Y.S., Chang, C.N., Chiang, Y.P., Sung, H.F., Chao, A.C., 2008. Photocatalytic degradation of lignin using Pt/TiO_2 as the catalyst. Chemosphere 71, 998–1004. https://doi.org/10.1016/j.chemosphere.2007.10.061.

MacHado, A.E.H., Furuyama, A.M., Falone, S.Z., Ruggiero, R., Perez, D.D.S., Castellan, A., 2000. Photocatalytic degradation of lignin and lignin models, using titanium dioxide: the role of the hydroxyl radical. Chemosphere 40, 115–124. https://doi.org/10.1016/S0045-6535(99)00269-6.

Makhotkina, O.A., Preis, S.V., Parkhomchuk, E.V., 2008. Water delignification by advanced oxidation processes: homogeneous and heterogeneous Fenton and H_2O_2 photo-assisted reactions. Appl. Catal. B Environ. 84, 821–826. https://doi.org/10.

1016/j.apcatb.2008.06.015.
Mialocq, J., Sutton, J., Goujon, P., 1980. Picosecond study of electron ejection in aqueous phenol and phenolate solutions. J. Chem. Phys. 72, 6338–6345.
Nair, V., Dhar, P., Vinu, R., 2016. Production of phenolics via photocatalysis of ball milled lignin-TiO_2 mixtures in aqueous suspension. RSC Adv. 6, 18204–18216. https://doi.org/10.1039/c5ra25954a.
Niu, K., Chen, P., Zhang, X., Tan, W.S., 2009. Enhanced enzymatic hydrolysis of rice straw pretreated by alkali assisted with photocatalysis technology. J. Chem. Technol. Biotechnol. 84, 1240–1245. https://doi.org/10.1002/jctb.2185.
Portjanskaja, E., Stepanova, K., Klauson, D., Preis, S., 2009. The influence of titanium dioxide modifications on photocatalytic oxidation of lignin and humic acids. Catal. Today 144, 26–30. https://doi.org/10.1016/j.cattod.2008.12.021.
Prado, R., Erdocia, X., Labidi, J., 2013. Effect of the photocatalytic activity of TiO_2 on lignin depolymerization. Chemosphere 91, 1355–1361. https://doi.org/10.1016/j.chemosphere.2013.02.008.
Saratale, R.G., Noh, H.S., Song, J.Y., Kim, D.S., 2014. Influence of parameters on the photocatalytic degradation of phenolic contaminants in wastewater using TiO_2/UV system. J. Environ. Sci. Health A 49, 1542–1552. https://doi.org/10.1080/10934529.2014.938532.
Sheng, J., Li, X., Xu, Y., 2014. Generation of H_2O_2 and OH radicals on Bi_2WO_6 for phenol degradation under visible light. ACS Catal. 4, 732–737. https://doi.org/10.1021/cs400927w.
Song, S., Xu, L., He, Z., Chen, J., Xiao, X., Yan, B., 2007. Mechanism of the photocatalytic degradation of C.I. reactive black 5 at pH 12.0 using $SrTiO_3$/CeO_2 as the catalyst. Environ. Sci. Technol. 41, 5846–5853. https://doi.org/10.1021/es070224i.
Song, L., Zhao, X., Cao, L., Moon, J.W., Gu, B., Wang, W., 2015. Synthesis of rare earth doped TiO_2 nanorods as photocatalysts for lignin degradation. Nanoscale 7, 16695–16703. https://doi.org/10.1039/c5nr03537f.
Subramanian, V., Wolf, E.E., Kamat, P.V., 2004. Catalysis with TiO_2/gold nanocomposites. Effect of metal particle size on the Fermi level equilibration. J. Am. Chem. Soc. 126, 4943–4950. https://doi.org/10.1021/ja0315199.
Sun, Z., Zhang, C., Chen, P., Zhou, Q., Hoffmann, M.R., 2017. Impact of humic acid on the photoreductive degradation of perfluorooctane sulfonate (PFOS) by UV/Iodide process. Water Res. 127, 50–58. https://doi.org/10.1016/j.watres.2017.10.010.
Tryba, B., Morawski, A.W., Inagaki, M., Toyoda, M., 2006. The kinetics of phenol decomposition under UV irradiation with and without H_2O_2 on TiO_2, Fe-TiO_2 and Fe-C-TiO_2 photocatalysts. Appl. Catal. B Environ. 65, 86–92. https://doi.org/10.1016/j.apcatb.2005.12.015.
Tsapekos, P., Kougias, P.G., Vasileiou, S.A., Lyberatos, G., Angelidaki, I., 2017. Effect of micro-aeration and inoculum type on the biodegradation of lignocellulosic substrate. Bioresour. Technol. 225, 246–253. https://doi.org/10.1016/j.biortech.2016.11.081.
Tsapekos, P., Alvarado-Morales, M., Boscaro, D., Mazarji, M., Sartori, L., Angelidaki, I., 2018. TiO_2-AgCl based nanoparticles for photocatalytic production of phenolic compounds from lignocellulosic residues. Energy Fuel 32, 6813–6822. https://doi.org/10.1021/acs.energyfuels.8b00572.
Upadhyay, R.K., Soin, N., Roy, S.S., 2014. Role of graphene/metal oxide composites as photocatalysts, adsorbents and disinfectants in water treatment: a review. RSC Adv. 4, 3823–3851. https://doi.org/10.1039/c3ra45013a.
Villaseñor, J., Mansilla, H.D., 1996. Effect of temperature on kraft black liquor degradation by ZnO-photoassisted catalysis. J. Photochem. Photobiol. A Chem. 93, 205–209. https://doi.org/10.1016/1010-6030(95)04179-6.
Wang, P.Q., Bai, Y., Luo, P.Y., Liu, J.Y., 2013. Graphene-WO3 nanobelt composite: elevated conduction band toward photocatalytic reduction of CO_2 into hydrocarbon fuels. Catal. Commun. 38, 82–85. https://doi.org/10.1016/j.catcom.2013.04.020.
Wang, X., Huang, S., Zhu, L., Tian, X., Li, S., Tang, H., 2014. Correlation between the adsorption ability and reduction degree of graphene oxide and tuning of adsorption of phenolic compounds. Carbon 69, 101–112. https://doi.org/10.1016/j.carbon.2013.11.070.
Wood, P.M., 1988. The potential diagram for oxygen at pH 7. Biochem. J. 253, 287–289.
Xu, Feng, Yu, Jianming, Tesso, Tesfaye, Dowell, Floyd, Wang, Donghai, 2013. Qualitative and quantitative analysis of lignocellulosic biomass using infrared techniques: a mini-review. Appl. Energy 104, 801–809. https://doi.org/10.1016/j.apenergy.2012.12.019.
Yang, W., Wen, Y., Chen, R., Zeng, D., Shan, B., 2014. Study of structural, electronic and optical properties of tungsten doped bismuth oxychloride by DFT calculations. Phys. Chem. Chem. Phys. 16, 21349–21355. https://doi.org/10.1039/c4cp02801e.
Yang, C., Li, Q., Tang, L., Xin, K., Bai, A., Yu, Y., 2015. Synthesis, photocatalytic activity, and photogenerated hydroxyl radicals of monodisperse colloidal ZnO nanospheres. Appl. Surf. Sci. 357, 1928–1938. https://doi.org/10.1016/j.apsusc.2015.09.140.
Zhang, L., Du, L., Cai, X., Yu, X., Zhang, D., Liang, L., Yang, P., Xing, X., Mai, W., Tan, S., Gu, Y., Song, J., 2013. Role of graphene in great enhancement of photocatalytic activity of ZnO nanoparticle-graphene hybrids. Physica E 47, 279–284. https://doi.org/10.1016/j.physe.2012.10.008.
Zhang, Q., Xu, M., You, B., Zhang, Q., Yuan, H., Ostrikov, K., 2018. Oxygen vacancy-mediated ZnO nanoparticle photocatalyst for degradation of methylene blue. Appl. Sci. 8, 353. https://doi.org/10.3390/app8030353.
Zhou, X., Shi, T., Zhou, H., 2012. Hydrothermal preparation of ZnO-reduced graphene oxide hybrid with high performance in photocatalytic degradation. Appl. Surf. Sci. 258, 6204–6211. https://doi.org/10.1016/j.apsusc.2012.02.131.